Xuan Nui Pham*
Huu-Tai Le
Trung-Tien Nguyen
Ngan-Thi Pham

Ag_3PO_4-Supported Magnetic Hydroxyapatite Composite as Green Photocatalyst for the Removal of Cationic and Anionic Dyes from Aqueous Solution

Eggshells were used as the main source for the synthesis of hydroxyapatite (HAp), and the semiconductor material Ag_3PO_4 was synthesized by the crystal formation process on magnetic HAp. X-ray diffraction, scanning electron microscopy, the Brunauer-Emmett-Teller surface area, and X-ray photoelectron, Fourier transform infrared, and ultraviolet-visible light diffuse reflectance spectroscopy were employed to study the phase structure, surface morphology, and optical properties of the composite photocatalyst. The photocatalytic activities of the synthesized composites were explored for the photodegradation of both cationic (Methylene Blue) and anionic (Reactive Red 195) dyes, achieving efficiencies of around 99 % and 96 %, respectively. Vibrating sample magnetometry showed the excellent regenerability of the magnetic composite after five cycles, demonstrating its potential for removing cationic and anionic dyes from aqueous solutions.

Keywords: Ag_3PO_4, Dye, Magnetic hydroxyapatite, Methylene Blue, Photocatalyst, Reactive Red 195

Received: June 03, 2021; *revised:* August 04, 2021; *accepted:* August 05, 2021

DOI: 10.1002/ceat.202100261

Supporting Information available online

1 Introduction

Nowadays, water pollution is a growing concern for industries such as the textile, paper, and pharmaceutical industries. Among them, the textile industry releases a significant amount of organic dyes every day. Due to the existence of many aromatic rings in the structures of these dyes that are highly resistant to chemical processes [1], their removal from wastewater with traditional biochemical and physicochemical methods is difficult [2]. Thus, advanced methods have been used, such as photocatalysis [3, 4], adsorption [5], and biological treatments [6]. The photocatalysis method is cost-effective and could degrade azo compounds under visible irradiation [7, 8]. Many researchers have focused on developing catalysts with low cost, narrow band gap energy, large surface area, high electron-hole pair separation efficiency, ease of fabrication, and operatability under visible light to improve the photodegradation efficiency [9–11].

Silver orthophosphate (Ag_3PO_4), known as a photocatalyst, has a relatively narrow band gap (2.36–2.43 eV). Therefore, as a highly efficient photocatalyst, Ag_3PO_4 has the ability to act as an antibacterial agent [12], oxidize water [13, 14] and decompose organic compounds in aqueous solutions under visible light irradiation [15]. However, an insurmountable problem for silver salts as semiconductor photocatalysts is their poor stability [16]. Also, photocorrosion of Ag_3PO_4 occurs during the absence of an electron acceptor in the photocatalytic process [17, 18]. Therefore, the advancement of the catalytic stability and activity of these silver-based semiconductor photocatalysts has become a critical task. Recently, more and more researches have focused on the proper support for the catalyst in order to enhance the application of composite photocatalysts. Ag_3PO_4 composite photocatalysts like Ag_3PO_4/SAPO-34 [19], Ag_3PO_4/$AlPO_4$-5 [20], Ag_3PO_4 and multiwalled carbon nanotubes [21], Ag_3PO_4 and graphene [22], and Ag_3PO_4/CNFs/silica fiber [23] are effective photocatalysts for Methylene Blue (MB) and Rhodamine B (RhB) degradation.

Hydroxyapatite (HAp) [$Ca_{10}(PO_4)_6(OH)_2$] is known as the main component of bone and teeth, belonging to the family of apatites [24]. It is one of the materials with excellent biocompatibility, bone-bonding properties, and filament induction [25]. HAp is a bioceramic that is mainly used in dentistry and bone regeneration applications due to its similarity with the inorganic components of bone [26]. Besides, HAp is used as an adsorbent of metal ions or organic substances such as nicotinic acid and phenol [27, 28]. However, the photocatalytic activity

Dr. Xuan Nui Pham, Dr. Huu-Tai Le, Dr. Trung-Tien Nguyen, Dr. Ngan-Thi Pham
phamxuannui@humg.edu.vn
Department of Chemical Engineering, Hanoi University of Mining and Geology, 18-Vien Street, Duc Thang Ward, Bac Tu Liem, 10000 Hanoi, Vietnam.

of an Ag_3PO_4-supported HAp composite is restricted due to the difficulty of its separation in practical applications. In order to overcome this problem, iron oxide minerals were added into the HAp support to make it easily recoverable by an external magnet [29]. Magnetite (Fe_3O_4) is known as the magnetic iron oxide; featuring no noxiousness and easy fabrication and separation, it has received considerable attention regarding its encapsulation among different catalysts [30].

This study aimed to evaluate the photocatalytic activity of an Ag_3PO_4-supported magnetic HAp catalyst composite (denoted as Ag_3PO_4/HAp@Fe_3O_4 hereafter) to degrade the cationic dye MB and the anionic dye Reactive Red 195 (RR 195) in aqueous solution under visible light irradiation. The composite HAp@Fe_3O_4 was synthesized by a simple coprecipitation method, and the Ag_3PO_4 nanoparticles were formed by deriving the phosphate ions from HAp. In addition, the effects of the photocatalyst dosage, the dye concentration, and the presence or absence of H_2O_2 on the degradation of the dyes and the recoverability of the composite Ag_3PO_4/HAp@Fe_3O_4 photocatalyst were also studied.

2 Experimental

2.1 Materials

Eggshells were collected from local sources in Vietnam. Silver nitrate ($AgNO_3$, > 99.98 %), iron(II) chloride tetrahydrate ($FeCl_2{\cdot}4H_2O$, ≥ 98 %), iron(III) chloride hexahydrate ($FeCl_3{\cdot}6H_2O$, ≥ 98 %), MB (≥ 97 %), and RR 195 (99 %) of analytical grade were purchased from Sigma-Aldrich. Phosphoric acid (H_3PO_4, 85 %), ammonia solution (NH_3, 28 %), and ethanol (C_2H_5OH, > 99.7 %) were purchased from Sinopharm Chemical Reagent Co. Ltd., China.

2.2 Synthesis of Materials

2.2.1 Synthesis of Magnetic HAp (HAp@γ-Fe_2O_3)

Eggshells were washed with deionized water to remove any odors and impurities. After pretreatment, they were finely ground to powder and calcined at 300 °C to remove organic components, then further heated at 900 °C to decompose $CaCO_3$ to CaO. The product was obtained in the form of a fine white powder.

H_3PO_4 (0.5 M, 100 mL) was added slowly into 100 mL solution containing 2.8 g CaO; the pH of the mixture was adjusted in the range of 10–12 using NH_3 solution under vigorous stirring and the resultant mixture was marked as mixture A. Mixture B contains 0.37 g $FeCl_2{\cdot}4H_2O$ and 1.0 g $FeCl_3{\cdot}6H_2O$ dissolved under vacuum in deionized water at 80 °C with vigorous magnetic stirring. The pH of mixture B was maintained between 9 and 10. After 2 h, mixture A was added slowly into mixture B, and the resulting mixture was stirred vigorously for 1 h and then autoclaved for 48 h. After aging, the sample was dried at 60 °C for 48 h and calcined at 300 °C for 3 h. The obtained product has the light brown color of maghemite.

2.2.2 Synthesis of Ag_3PO_4-Supported Magnetic HAp (Ag_3PO_4/HAp@γ-Fe_2O_3)

Four different amounts of $AgNO_3$ (0.1, 0.15, 0.203, and 0.254 g, corresponding to the weight percentages of Ag_3PO_4 of 20, 30, 40, and 50 wt %, respectively, were dissolved in distilled water. Firstly, 4.0 g magnetic HAp was dispersed in 200 mL H_2O and the suspension was stirred intensively for 15 min. Then, a particular amount of silver nitrate solution was added dropwise into the stirred magnetic HAp suspension. After reacting for 5 h, the precipitates were separated by a permanent magnet, washed with distilled water and dried at 60 °C under vacuum for 24 h. The obtained composites were labeled as 20 %, 30 %, 40 %, and 50 % Ag_3PO_4/HAp@γ-Fe_2O_3.

2.3 Characterization

The crystal lattice structure of the synthesized samples was determined by X-ray powder diffraction (XRD) using a D8 Advance system (CuKα_1 copper radiation, $\lambda = 0.154$ nm, 3° min^{-1} scanning speed; Bruker, Germany). The surface morphology was observed by a scanning electron microscope (S-4800, Hitachi). The Fourier transform infrared (FT-IR) spectra were measured with an FT-IR Affinity-1S (Shimadzu). Ultraviolet-visible light diffuse reflectance spectroscopy (UV-vis DRS) was performed with the UV-2600 spectrophotometer from Shimadzu. The Brunauer-Emmett-Teller (BET) specific surface area was determined at the temperature of liquid nitrogen (77 K) using the N_2 adsorption-desorption technique on a ChemBET-3030 system. X-ray photoelectron spectroscopy (XPS) was conducted using an ESCALab 250 spectrometer (Thermo VG, UK). Vibrating sample magnetometry (VSM) was measured on the DMS 880 VSM 100/700 K magnetometer.

2.4 Point of Zero Charge Determination Method

The point of zero charge (PZC) of Ag_3PO_4/HAp@γ-Fe_2O_3 was measured by the salt addition method [31]. Typically, 50 mg of each sample was dispersed in 50 mL 0.1 M KCl in 100-mL glass Erlenmeyer flasks by magnetic stirring for 30 min. The initial pH values (pH_0) of the suspension were adjusted to several values between 2 and 12 by adding either 0.25 M HCl or NaOH solution, measured by a calibrated Hach pHC201 pH meter with an accuracy of ± 0.02. After shaking for 24 h in a revolving water bath to reach equilibrium, the resulting pH values were measured. The difference between the initial and final pH values ($\Delta pH = pH - pH_0$) against the initial pH was plotted. The pH value where ΔpH was zero was taken as the PZC.

2.5 Photocatalytic Activity and Active-Species Trapping Experiments

The activity of the Ag_3PO_4/HAp@γ-Fe_2O_3 magnetic photocatalyst was evaluated through the ability to degrade the cationic dye MB and the anionic dye RR 195 under visible irradiation.

The degradation process was performed as follows: 50 mg of the catalyst was dispersed in the dye solution (30 mL, 50 ppm). The solution mixture was placed in the dark for 60 min to reach the adsorption-desorption equilibrium. Then, it was irradiated by a 125-W Xe lamp and 0.5 mL H_2O_2 as an oxidant was added to the mixture. After each hour, 3-mL samples were taken and centrifuged to recover the catalysts. The samples were analyzed using a UV-Vis 2450 spectrometer at a maximum wavelength of $\lambda = 664$ nm for MB and $\lambda = 541$ nm for RR 195. The active species in the photocatalytic process could be identified by a trapping experiment with *tert*-butyl alcohol (TBA), potassium dichromate ($K_2Cr_2O_7$), ammonium oxalate monohydrate (AO), and 1,4-benzoquinone (BQ), which was similar to the photodegradation experiment except that a number of scavengers were added into the dye solution at the beginning of the irradiation. All the experiments were performed under ambient conditions.

The conversion of the dye was calculated based on its initial concentration, C_0 (mg L^{-1}), and the concentration C_t (mg L^{-1}) of dyes in the solution at reaction time t (min).

$$A = \left[\frac{(C_0 - C_t)}{C_0}\right] \times 100 \quad (1)$$

where A is the conversion (%) of the dye(s).

3 Results and Discussion

3.1 Characterization of the Samples

The crystal and chemical structures of the synthesized materials including HAp, HAp@γ-Fe_2O_3, and the 20–50 % Ag_3PO_4/HAp@γ-Fe_2O_3 composites were characterized by XRD. The results are shown in Fig. 1.

Characteristic diffraction peaks of the apatite phase in the HAp structure were observed at $2\theta = 25.9°$, 31.77°, 32.87°, 34.04°, 49.5°, and 53.10°, corresponding to the (002), (211), (300), (202), (213), and (004) planes (JCPDS 09-0432). With the HAp@γ-Fe_2O_3 sample, the peak intensity of HAp decreases due to the coverage on the surface. Furthermore, characteristic peaks of γ-Fe_2O_3 appeared at $2\theta = 35.7°$ and 53.3°, corresponding to the magnetic diffraction (311) and (422), respectively, of the maghemite crystal planes (JCPDS 39-1346). The Ag_3PO_4 photocatalyst was successfully synthesized using HAp as a source of phosphate ions. Typical diffraction peaks of Ag_3PO_4 were observed at $2\theta = 20.9°$, 29.7°, 33.4°, 36.7°, 47.9°, 52.9°, 55.2°, and 61.92°, corresponding to the (110), (200), (210), (211), (310), (222), (320), and (400) crystal planes, respectively (JCPDS 06-0505). These diffraction peaks can be indexed to the pure body-centered cubic (bcc) structure of Ag_3PO_4 [32]. In Fig. 1b, the diffraction peaks of Ag_3PO_4 were sharper along with a higher intensity when the Ag_3PO_4 content increased from 20 % to 50 %, indicating that Ag_3PO_4 accumulated more on HAp@γ-Fe_2O_3. This result is consistent with the previous study of Gan et al. [33].

HAp@γ-Fe_2O_3 and the composite samples were measured with FT-IR spectroscopy to confirm the chemical structures. In Fig. 2, the peaks at 566 and 602 cm^{-1} were assigned to υ_4 of a triply degenerate bending mode of $(PO_4)^{3-}$. The characteristic peaks at 1029 and 1096 cm^{-1} were attributed to a triply degenerate asymmetric stretching mode (υ_3) of $(PO_4)^{3-}$ in HAp. The peak at 966 cm^{-1} was due to the non-degenerate symmetric stretching mode (υ_1) of the $(PO_4)^{3-}$ group [19, 20]. The peaks at 1639 cm^{-1} were attributed to OH^-. Furthermore, the absorption peak at 1458 cm^{-1} was a characteristic band of CO_3^{2-}, which may be due to air in the synthesis process [34]. Typical

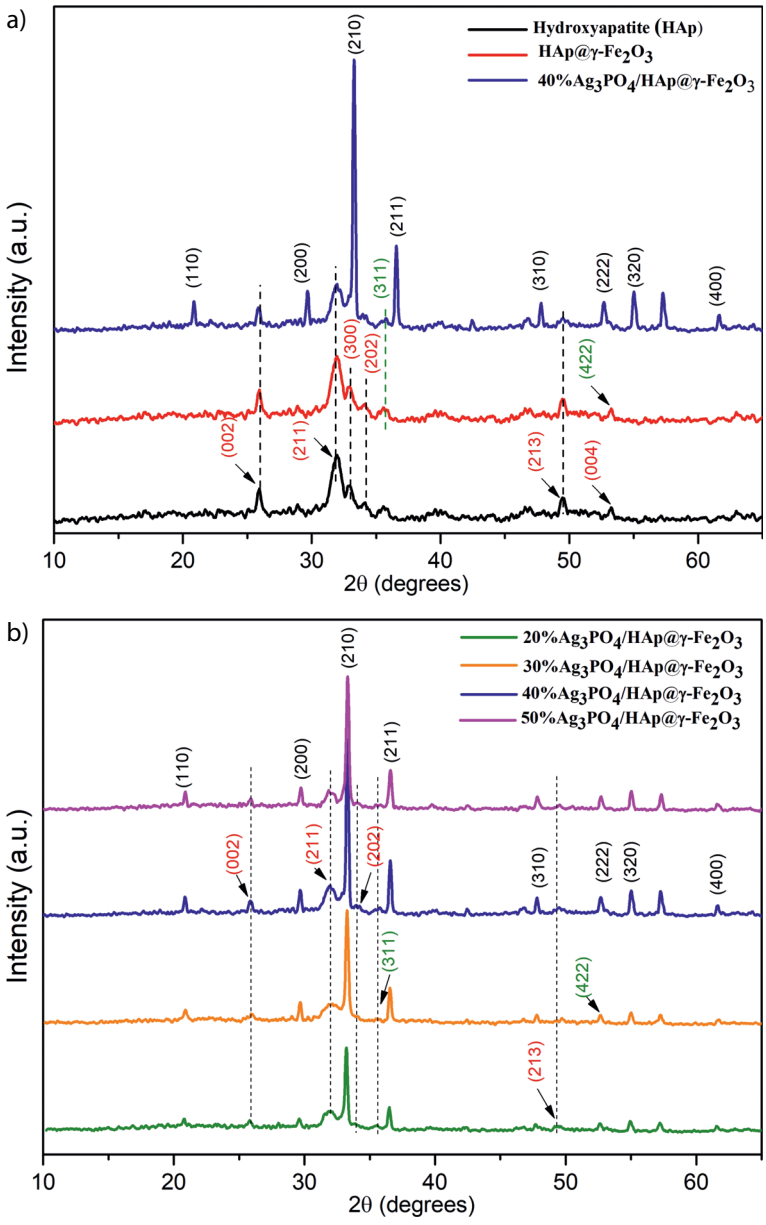

Figure 1. XRD patterns of (a) pure HAp, HAp@γ-Fe_2O_3, 40 % Ag_3PO_4/HAp@γ-Fe_2O_3, and (b) the 20–50 % Ag_3PO_4/HAp@γ-Fe_2O_3 composites.

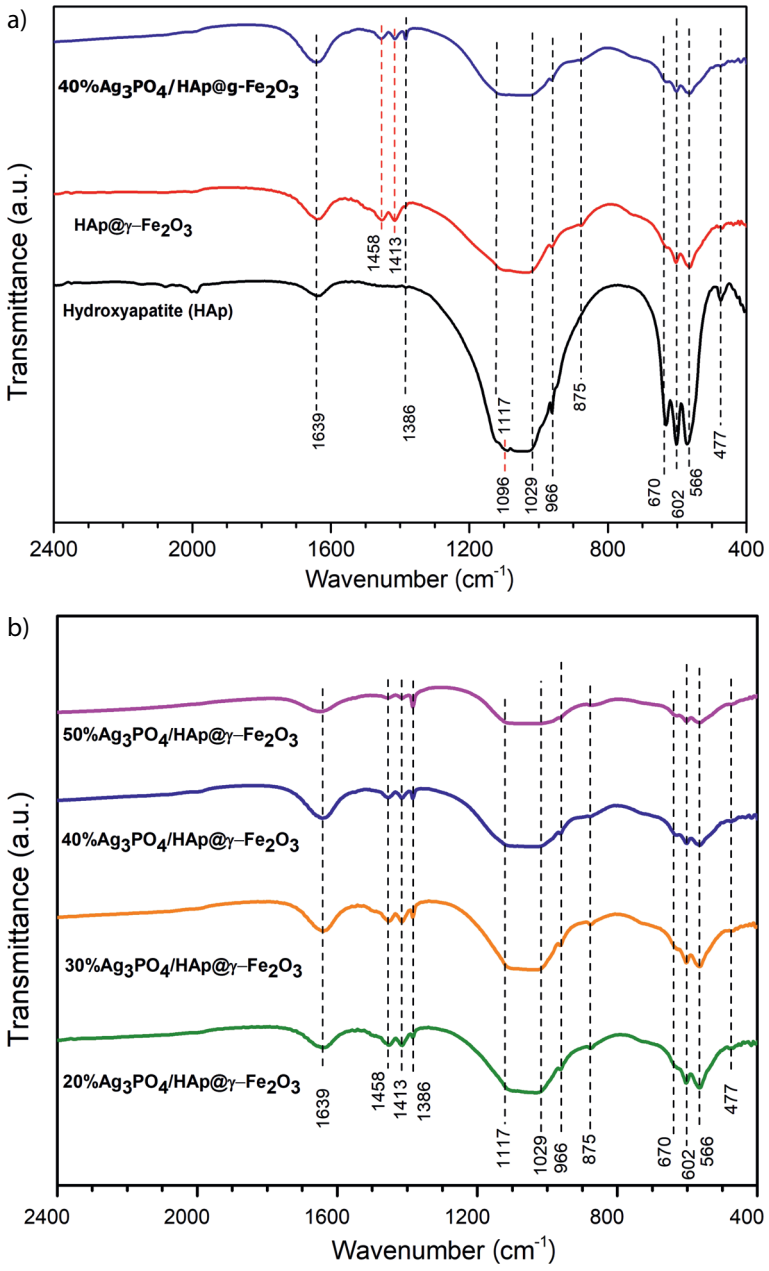

Figure 2. FT-IR spectra of (a) pure HAp, HAp@γ-Fe_2O_3, 40 % Ag_3PO_4/HAp@γ-Fe_2O_3, and (b) the 20–50 % Ag_3PO_4/HAp@γ-Fe_2O_3 composites.

absorption bands of γ-Fe_2O_3 were in the range of 450–640 cm^{-1} [35]. The peaks at 875 and 1117 cm^{-1} confirm the chemisorption of HAp onto the γ-Fe_2O_3 surface [10]. For the Ag_3PO_4/HAp@γ-Fe_2O_3 composites, no characteristic vibrations of Ag_3PO_4 were observed, due to the similar chemical structures of Ag_3PO_4 and HAp [36].

The specific surface areas and pore sizes of HAp@γ-Fe_2O_3 and 40 % Ag_3PO_4/HAp@γ-Fe_2O_3 were determined by using the N_2 adsorption-desorption and Barrett-Joyner-Halenda (BJH) methods (Fig. 3 and Tab. 1).

The N_2 adsorption-desorption isotherm of HAp@γ-Fe_2O_3 and 40 % Ag_3PO_4/HAp@γ-Fe_2O_3 was a type-IV isotherm. The hysteresis curves were of type H_4, characteristic of a uniform size and a cylindrical pore shape. The surface area of the HAp@γ-Fe_2O_3 support was 56.96 m^2g^{-1}, significantly lower than that of Ag_3PO_4/HAp@γ-Fe_2O_3 with 74.33 m^2g^{-1}. The formation of Ag_3PO_4 crystals on the surface of HAp had increased the surface area. However, silver phosphate crystal formation slightly reduced the pore volume, from 0.48 to 0.36 cm^3g^{-1}, and the pore size also decreased from 33.68 to 19.34 nm.

Scanning electron microscopy (SEM) and transmission electron microscopy (TEM) were performed to analyze the structural and morphological characteristics of HAp, HAp@γ-Fe_2O_3, and the 40 % Ag_3PO_4/HAp@γ-Fe_2O_3 photocatalyst (Fig. 4). The SEM image of HAp is shown in Fig. 4a; it can be seen that HAp has a rod structure with a length of 200–300 nm. SEM of the HAp@γ-Fe_2O_3 and 40 % Ag_3PO_4/HAp@γ-Fe_2O_3 composites (Fig. 4b, c) show that the γ-Fe_2O_3 and Ag_3PO_4 nanoparticles could not be clearly observed through SEM. In addition, the TEM images of 40 % Ag_3PO_4/HAp@γ-Fe_2O_3 clearly show that the rod-shaped structure of HAp was interspersed with spherical nanoparticles of γ-Fe_2O_3 and Ag_3PO_4 nanoparticles were successfully immobilized on the surface of HAp@γ-Fe_2O_3.

XPS was performed to inspect the surface compositions and chemical states of the 40 % Ag_3PO_4/HAp@γ-Fe_2O_3 samples. The XPS results (Fig. 5a) show the presence of Ag, P, Ca, O, P, and Fe elements, and carbon impurities were observed in Ag_3PO_4/HAp@γ-Fe_2O_3. Fig. 5b shows the binding energy of Ag 3d with two peaks converging at 368.18 and 374.17 eV, corresponding to Ag $3d_{5/2}$ and Ag $3d_{3/2}$. This indicates the existence of the Ag^+ ion in Ag_3PO_4/HAp@γ-Fe_2O_3. The binding energy of 133.07 eV was assigned to P 2p (Fig. 5c). Two types of oxygen peaks appeared in the Ag_3PO_4/HAp@γ-Fe_2O_3 composite (Fig. 5d). The binding energy of 531.3 eV suggested that the oxygen originated from the non-bridging (P=O) oxygen atoms of Ag_3PO_4, whereas the binding energy of 532.9 eV indicated that the oxygen originated from the bridging oxygen atoms (P–O–Ag) and the adsorbed oxygen or water molecules [37]. Thus, the appearance of Ag species that exist in the

Table 1. BET specific surfaces (S_{BET}), pore volumes (V_p), and pore sizes (D) of HAp@γ-Fe_2O_3 and 40 % Ag_3PO_4/HAp@γ-Fe_2O_3.

Samples	S_{BET} [m^2g^{-1}]	V_p [cm^3g^{-1}]	D [nm][a)]
HAp@γ-Fe_2O_3	56.96	0.48	33.68/34.44
40 % Ag_3PO_4/HAp@γ-Fe_2O_3	74.13	0.36	19.34/19.53

[a)] The pore diameters were calculated from the adsorption/desorption branch of the isotherm using the BJH method.

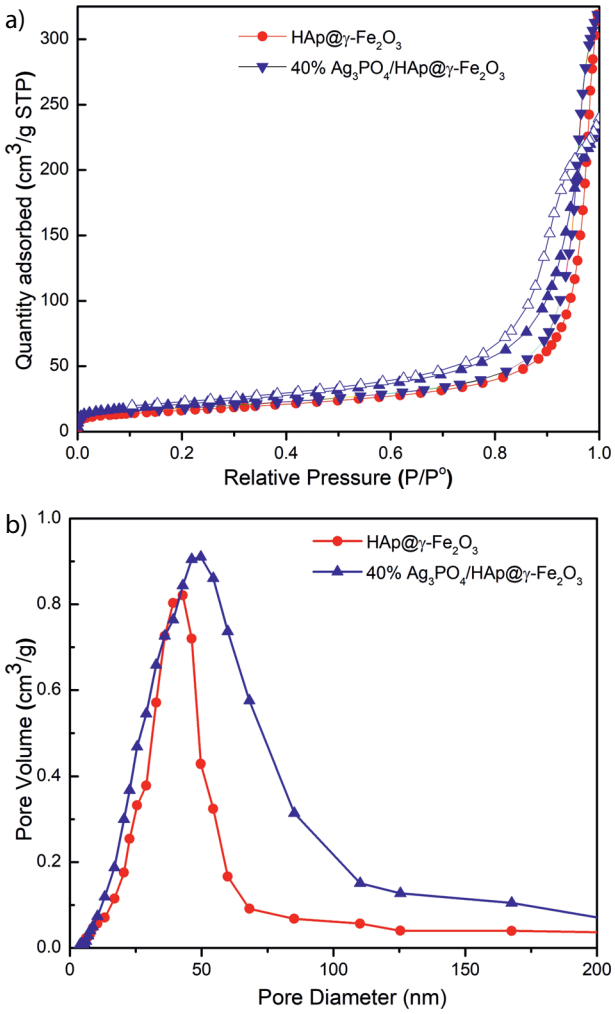

Figure 3. (a) N_2 adsorption-desorption isotherms and (b) pore size distribution (inset) of HAp@γ-Fe_2O_3 and 40 % Ag_3PO_4/HAp@γ-Fe_2O_3.

form of Ag^+ ions was confirmed. The XPS spectrum of Ca 2p (Fig. 5e) with two peaks of Ca $2p_{3/2}$ (347.1 eV) and Ca $2p_{1/2}$ (350.7 eV) characterizes the state of Ca 2p in HAp [38, 39]. In Fig. 5f, the binding energy was 710.7 eV, which characterizes the oxidized state of Fe^{3+}, as reported by Blomquist et al. [40]. This confirmed the absence of Fe(II) ions in the structure of γ-Fe_2O_3.

The absorbent properties of a semiconductor determine its photocatalytic activity. Thus, the UV-vis DRS method was carried out for the 20–50 % Ag_3PO_4/HAp@γ-Fe_2O_3 composite photocatalysts (Fig. 6a).

In previous reports, the absorption edge of pure Ag_3PO_4 was observed at 530 nm [12, 41], while the adsorption edge of the composites slightly shifted to the long-wavelength region. The absorption wavelengths of the 20–50 % Ag_3PO_4/HAp@γ-Fe_2O_3 composites were 635, 652, 708, and 673 nm, respectively. The band gap energies of the composites were calculated using the Kubelka-Munk equation [42].

$$\alpha h\nu = A\left(h\nu - E_g\right)^{n/2} \quad (2)$$

where E_g is the band gap of the semiconduction, A is the absorption constant, ϑ is the frequency of light (s^{-1}), and h is the Planck constant. The value of n was determined by the transition model of the semiconductor. In the previous study [43], $n = 1$ was determined by the indirect transition of semiconductors. For 20 %, 30 %, 40 %, and 50 % Ag_3PO_4/HAp@γ-Fe_2O_3, the band gap energy values were 1.95, 1.9, 1.75, and 1.84 eV, respectively. When the content of Ag_3PO_4 increased to 50 wt %, the band gap energy increased again, proving that, when Ag_3PO_4 entirely covered the surface of HAp, the band gap energy will gradually shift to the level of pure Ag_3PO_4, which was 2.33 eV. Also from the obtained results it was shown that, when Ag_3PO_4 nanoparticles were loaded onto the HAp@γ-Fe_2O_3 support, the band gap values were lower than those of pure silver phosphate. This could be due to the addition of maghemite nanoparticles which absorb sunlight. The light creates pairs of charge carriers in the composite photocatalyst, consisting of a negatively charged electron and a positive charge hole [44, 45], indicating that the use of the HAp@γ-Fe_2O_3 support as the precursor was a crucial factor in increasing the efficiency of the photocatalyst.

The charge separation of the catalysts was investigated by the analysis of room temperature photoluminance (PL) spectra. As shown in Fig. 7, all the photocatalysts show a broad PL emission peak centered at around 602 nm. It can be found that the PL emission intensities reach the maximum value for the 20 % Ag_3PO_4/HAp@γ-Fe_2O_3 composite and decrease significantly with the 30–50 % Ag_3PO_4/HAp@γ-Fe_2O_3 composites. Notably, the 40 % Ag_3PO_4/HAp@γ-Fe_2O_3 composite exhibits the lowest PL emission intensity, clearly demonstrating that the recombination of the photogenerated electron-hole pairs was effectively inhibited to increase the photocatalytic activity and performance yield.

3.2 Photocatalytic Activity

The isoelectric point is an essential factor of the surface and is closely related to the material adsorption properties. When the solids disperse in water with a pH value lower than the isoelectric pH, the material surface is positively charged due to H^+ ion adsorption in aqueous solution, resulting in ΔpH variation in positive solution and conversely. Fig. 8a shows the dependence of the ΔpH on the initial pH value (pH_i) of the photocatalytic composite. From Fig. 8a, the isoelectric point of 40 % Ag_3PO_4/HAp@γ-Fe_2O_3 was determined to be 6.8. Hence, the composite can adsorb both anionic and cationic dyes.

Fig. 8b illustrates the photocatalytic performance degradation of RR 195 and MB using the 40 % Ag_3PO_4/HAp@γ-Fe_2O_3 composite under visible light irradiation for 4 h. The results show that the photodegradation of RR 195 reached 96.82 % after 4 h, and the MB dye was completely degraded within 3 h, indicating that 40 % Ag_3PO_4/HAp@γ-Fe_2O_3 could efficiently harvest sunlight to drive the photocatalytic reaction. This is entirely consistent with the value obtained from the isoelectric point on the surface of HAp@γ-Fe_2O_3 with $pH_{PZC} = 6.8$. The HAp@γ-Fe_2O_3 surface is thus positively charged in acidic pH (pH < 6.8) and negatively charged in alkaline pH (pH > 6.8). The obtained results in Fig. 8b showed that the

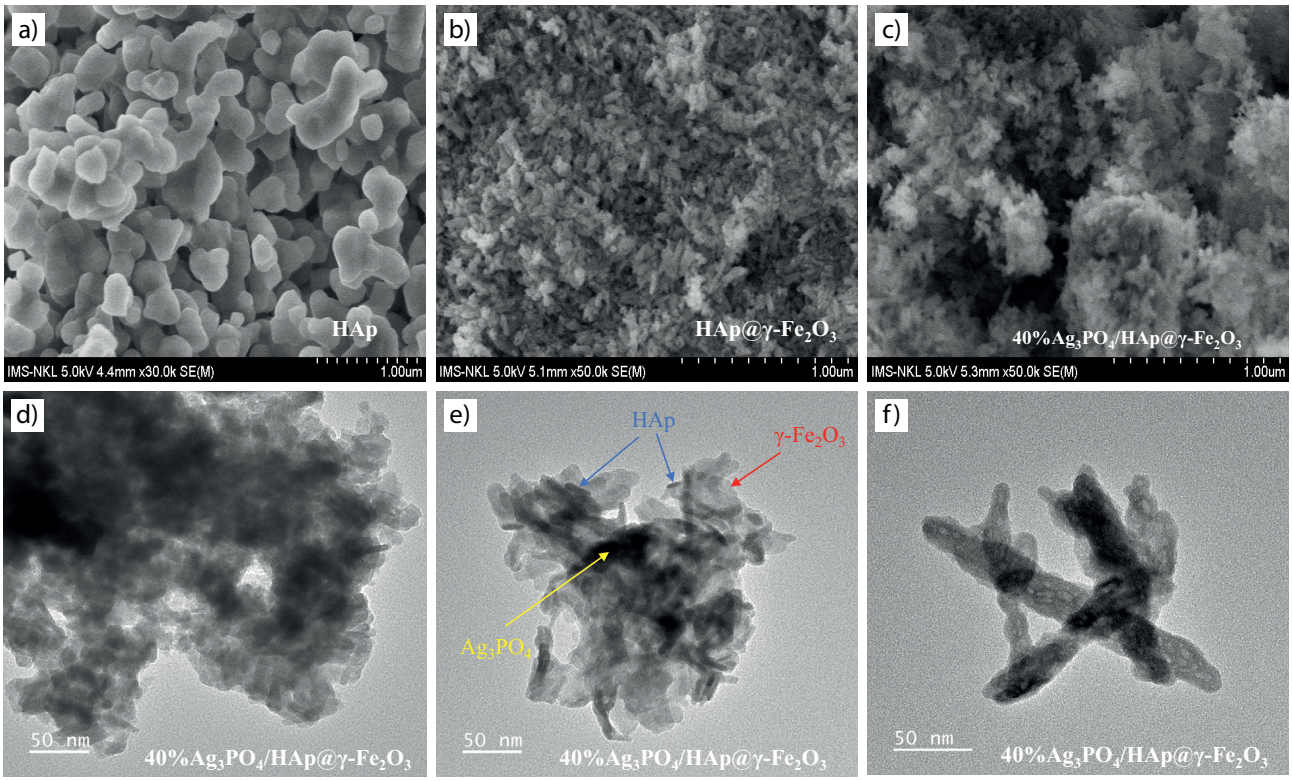

Figure 4. SEM images of (a) HAp, (b) HAp@γ-Fe_2O_3, (c) the 40 % Ag_3PO_4/HAp@γ-Fe_2O_3 composite; (d–f) TEM images of the 40 % Ag_3PO_4/HAp@γ-Fe_2O_3 composite.

Ag_3PO_4/HAp@γ-Fe_2O_3 photocatalyst has a high degradation efficiency with both the MB and RR 195 dyes. However, as RR 195 has a complex structure and a longer degradation time than MB, RR 195 was chosen as the model dye to evaluate the factors affecting the photocatalytic efficiency of Ag_3PO_4/HAp@γ-Fe_2O_3. Additionally, looking at the supplementary data (see Supporting Information Tab. S1), the performance of Ag_3PO_4/HAp@γ-Fe_2O_3 in this study is comparable to or far outweighs those of other materials such as O-*g*-C_3N_4/H-ZSM-5 [10], Fe-AO-*n*-PAN [46], or Ag_3PO_4/Ag [32], which were tested under similar conditions.

3.2.1 Effect of the Ag_3PO_4 Contents

The photocatalytic activities of the 20–50 % Ag_3PO_4/HAp@γ-Fe_2O_3 composites were evaluated by the degradation of RR 195 in aqueous solution (30 mL) under visible light irradiation. Before the Xe lamp irradiation, the mixture containing the Ag_3PO_4/HAp@γ-Fe_2O_3 and RR 195 solution was magnetically stirred for 1 h in the dark to reach the adsorption-desorption equilibrium. Fig. 9a shows that the Ag_3PO_4/HAp@γ-Fe_2O_3 composite with 40 % Ag_3PO_4 exhibited the highest photocatalytic activity, degrading 96.82 % of RR 195 after 4 h of irradiation. However, when the Ag_3PO_4 content reached 50 %, the degradation efficiency was reduced to 88.83 %. Due to an increase in the active-phase content, the Ag_3PO_4 nanoparticles agglomerated, thereby reducing the penetration of light into the inner layer of the solution. It can be assumed that the reduction in catalytic activity is due to the shielding effect of the catalyst [47–49]. Therefore, 40 % Ag_3PO_4/HAp@γ-Fe_2O_3 was determined to be the optimal active-phase dose, which was used in the subsequent experiments.

3.2.2 Effect of the RR 195 Concentration

The effect of the initial concentration of RR 195 on the photocatalytic activity was investigated with concentrations ranging from 30 to 90 ppm under visible light (Fig. 9b). The dye degradation efficiency depended on the initial concentration of RR 195. For example, 50 ppm of RR 195 shows the highest degradation efficiency at 96.82 %; when the initial concentration of RR 195 increased from 50 to 90 ppm, the photocatalytic efficiency decreased from 96.82 % to 82 %. The obtained results show that the photocatalyst had a high adsorption ability with low concentrations of RR 195; this could be due to the larger surface area of the photocatalyst material. Furthermore, increasing the dye concentration will stimulate the interaction between the initial dye molecules and forms the intermediate products of the adsorption process. Pare et al. [50] suggested that, when the irradiation time and catalyst content are constant, $^{\bullet}O_2$ radical formation on the catalyst surface decreases with increasing initial dye concentration.

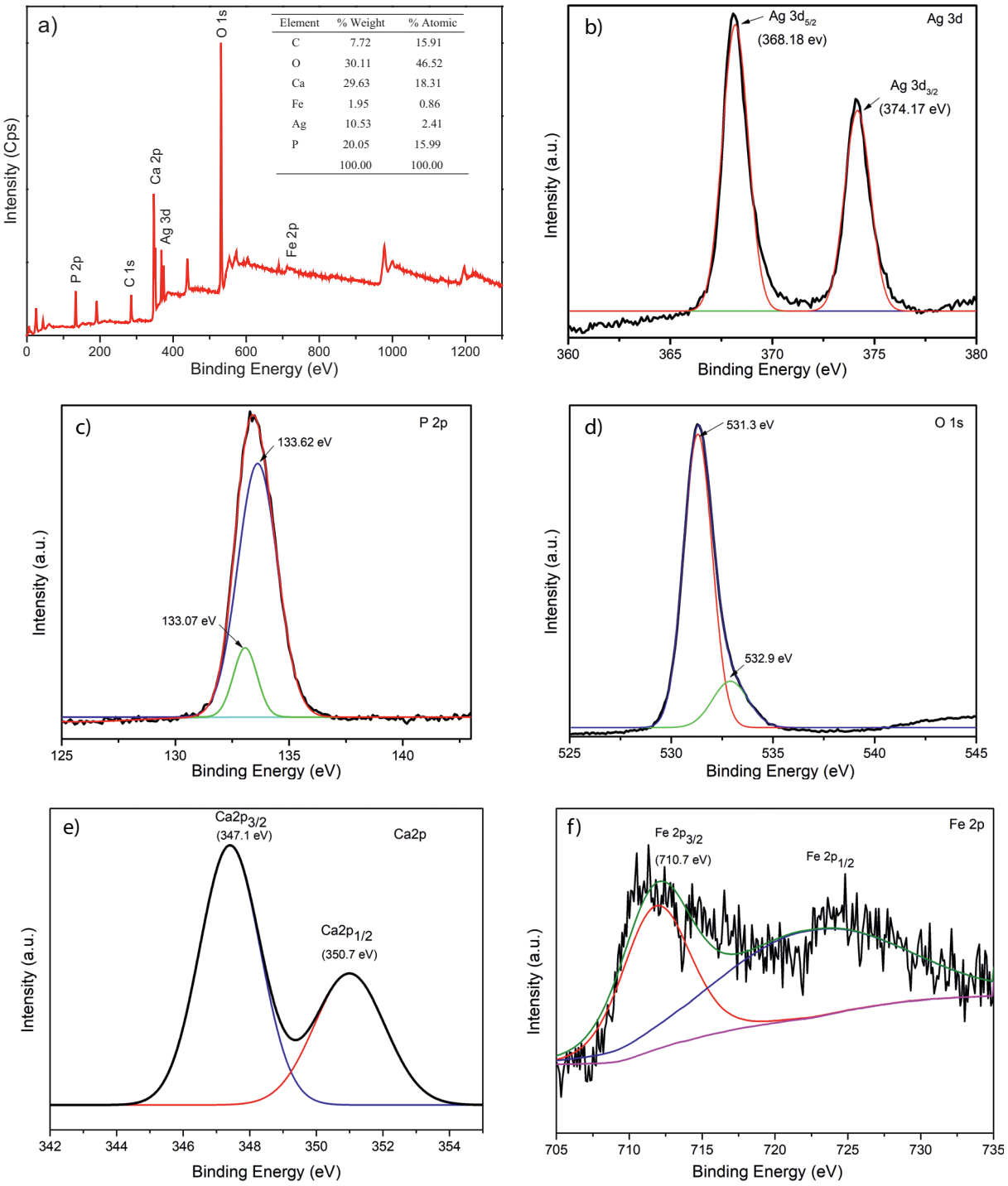

Figure 5. XPS spectrum of the 40 % Ag_3PO_4/HAp@γ-Fe_2O_3 composite photocatalysts: (a) survey scan, (b) Ag 3d, (c) P 2p, (d) O 1s, (e) Ca 2p, and (f) Fe 2p.

3.2.3 Effect of an Oxidizing Agent on the Photodegradation of RR 195

From the quantum point of view, the low quantum efficiency is due to the rapid recombination between photogenerated electron-hole pairs. The oxidant H_2O_2 was added to the reaction system to prevent this recombination. H_2O_2 can act as scavenger of electrons that were produced during photocatalysis. The OH^- ion that was produced from the decomposition reaction of H_2O_2 under light in turn reacts with holes (h^+), thus restricting the recombination of electrons and holes in the molecular orbital of the photocatalyst [51, 52]. In additon,

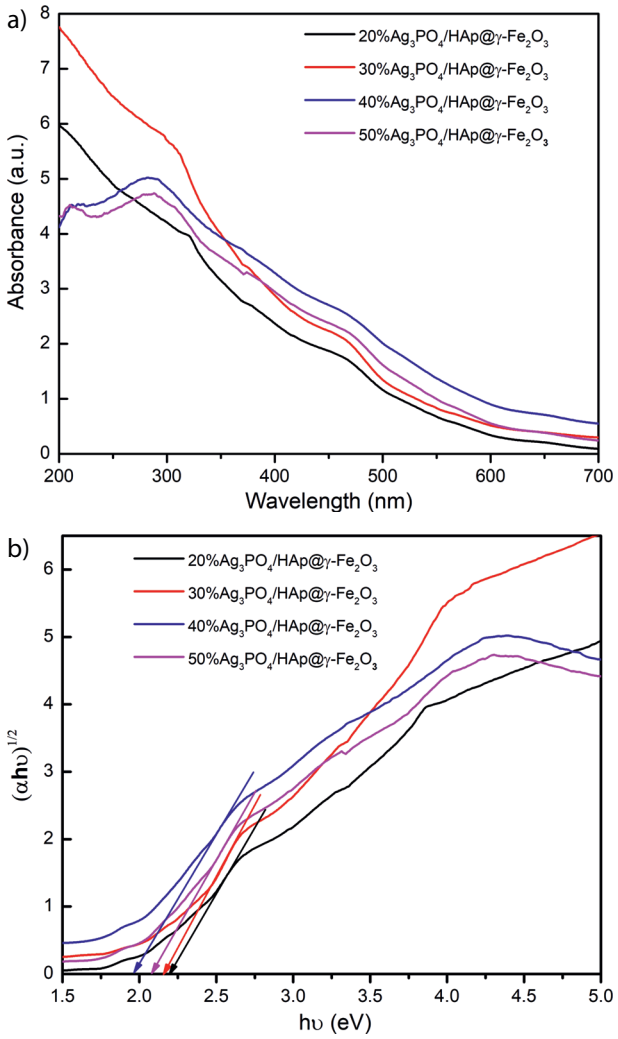

Figure 6. (a) UV-vis diffuse reflectance spectra, (b) Kubelka-Munk plot of the 20–50 % Ag_3PO_4/HAp@γ-Fe_2O_3 composites.

H_2O_2 can also act as the source of oxidation because it consumes conduction band electrons to form active valence band holes that oxidize RR 195. The reaction between conduction band electrons formed free radical anions ($^{\bullet}O_2^-$ and $^{\bullet}OH$). Fig. 9c shows that 96.82 % of RR 195 was degraded using the oxidant H_2O_2. However, the conversion of RR 195 under the same conditions also reached 92.82 % without using H_2O_2. The decrease in the conversion rate during the photodegradation of RR 195 was negligible when using the 40 % Ag_3PO_4/HAp@γ-Fe_2O_3 photocatalyst. Phosphorus addition in the structure of Ag_3PO_4 appears to have adjusted both its structure and oxidation capacity, and thus led to higher photooxidation by Ag_3PO_4 under visible light irradiation [15]. Moreover, the 40 % Ag_3PO_4/HAp@γ-Fe_2O_3 composite released silver ions, which were reduced by photoexcited electrons and led to the rapid carrier (electrons-holes) separation, both with and without H_2O_2 [53].

3.3 Reusability

The recyclability and reusability of composite photocatalysts are essential for practical applications. Fig. 10a shows the degradation of RR 195 using the photocatalyst. After the first degradation cycle, the photocatalyst was collected by an external magnet and used for the next cycles. The catalytic efficiency of 40 % Ag_3PO_4/HAp@γ-Fe_2O_3 remained at over 90 % after five consecutive uses, indicating the high reusability of the Ag_3PO_4/HAp@γ-Fe_2O_3 composite.

The magnetic stability of the photocatalyst was measured by VSM. The obtained results from Fig. 10b show that the saturation magnetization of Ag_3PO_4/HAp@γ-Fe_2O_3 before and after the five recycles were 2.9 and 2.7 emu g^{-1}, respectively, at a magnetic field of 10 000 Oe, implying that the magnetic response to the magnetic field was maintained.

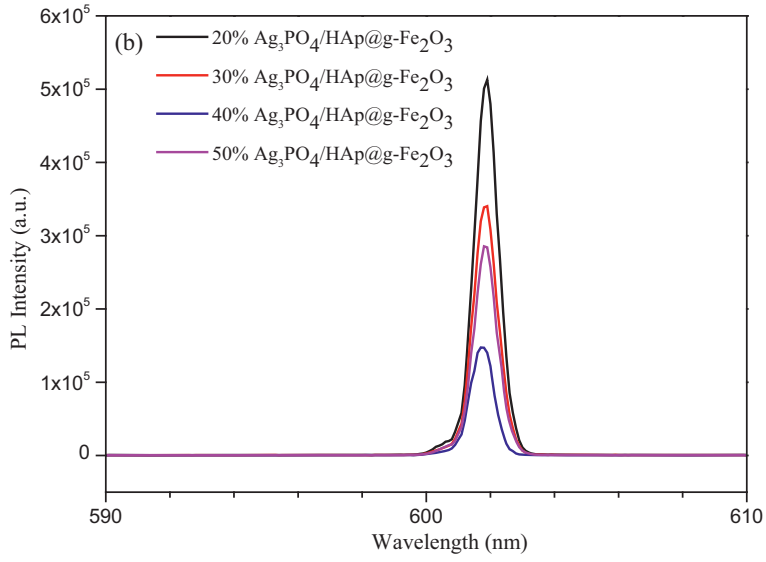

Figure 7. Photoluminescence spectra of the 20–50 % Ag_3PO_4/HAp@γ-Fe_2O_3 composites.

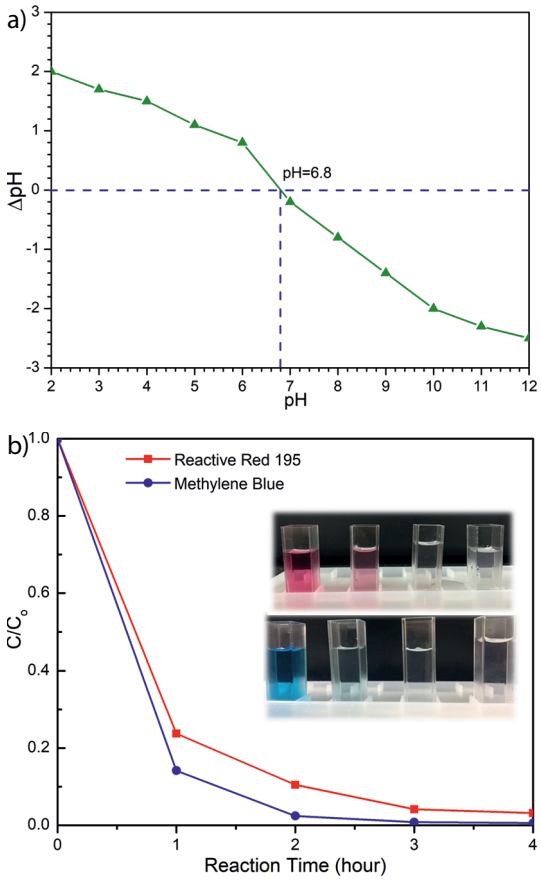

Figure 8. (a) PZC for the Ag_3PO_4/HAp@γ-Fe_2O_3 composite; (b) RR 195 and MB photocatalytic degradation over the 40 % Ag_3PO_4/HAp@γ-Fe_2O_3 photocatalyst under visible light irradiation. Reaction conditions: V_{sample} = 25 mL, $m_{photocatalyst}$ = 50 mg, 0.5 mL H_2O_2.

3.4 Mechanism of Photocatalytic Degradation of MB and RR 195

The trapping experiment of various active species was investigated by photodegradation of the MB and RR 195 dyes. BQ, AO, TBA, and $K_2Cr_2O_7$ were used as the superoxide radical ($^{\bullet}O_2^-$), hole (h^+) scavenger, hydroxyl radical ($^{\bullet}OH$), and electron (e|_) scavenger, respectively. As shown in Fig. 11a,b, the maximum values of photodegradation of MB and RR 195 were achieved in the absence of quenchers. The introduction of TBA and $K_2Cr_2O_7$ leads to a negligible effect on the photodegradation of MB and RR 195, indicating that $^{\bullet}OH$ and e|_ are also minor activated species in the photodegradation of cationic (MB) and anionic (RR 195) dyes. In contrast, the addition of BQ significantly suppresses the photodegradation activity of the Ag_3PO_4/HAp@γ-Fe_2O_3 composite, revealing that the superoxide radical plays a crucial role in the photocatalytic process. The addition of AO also slightly decreases the photocatalytic activity of the dyes. From this, it was confirmed that $^{\bullet}O_2^-$ was responsible for the MB and RR 195 degradation.

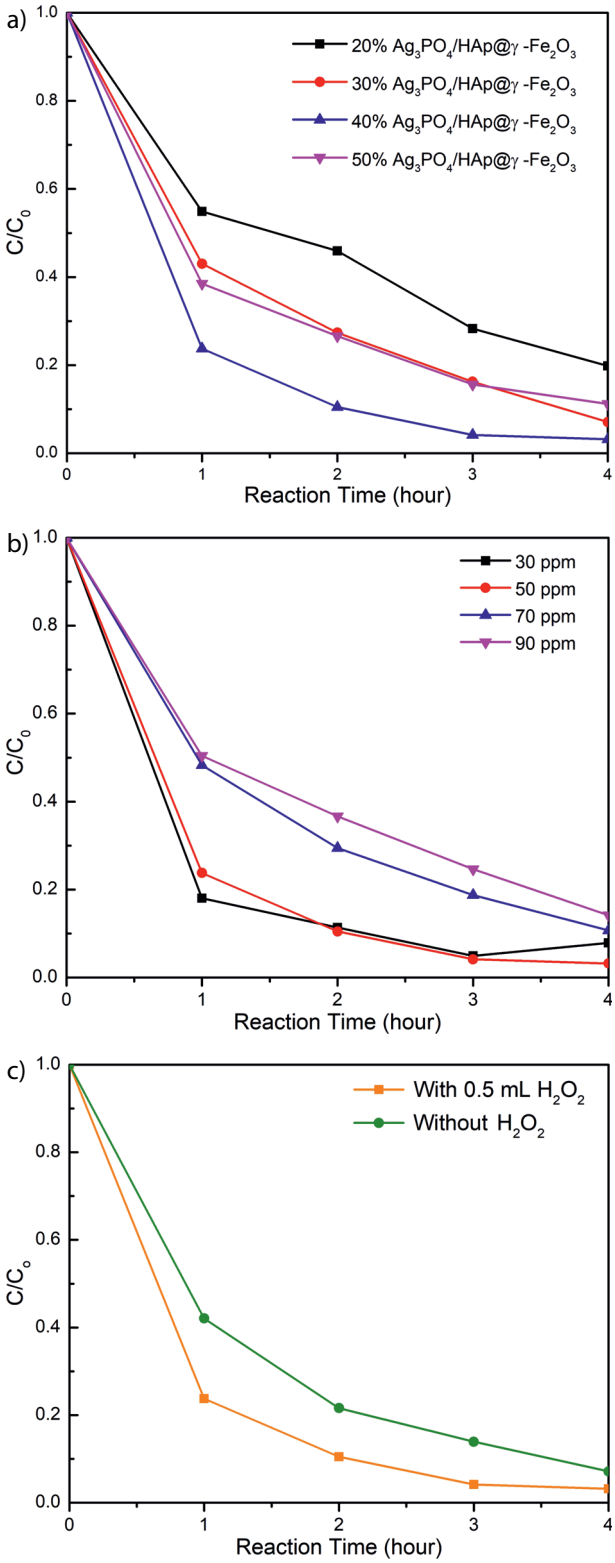

Figure 9. Photodegradation of RR 195 under various reaction conditions of (a) photocatalysts, (b) concentration of the RR 195, (c) without H_2O_2 and with 0.5 mL H_2O_2. Reaction conditions: V_{sample} = 30 mL, $m_{photocatalyst}$ = 50 mg, 0.5 mL H_2O_2.

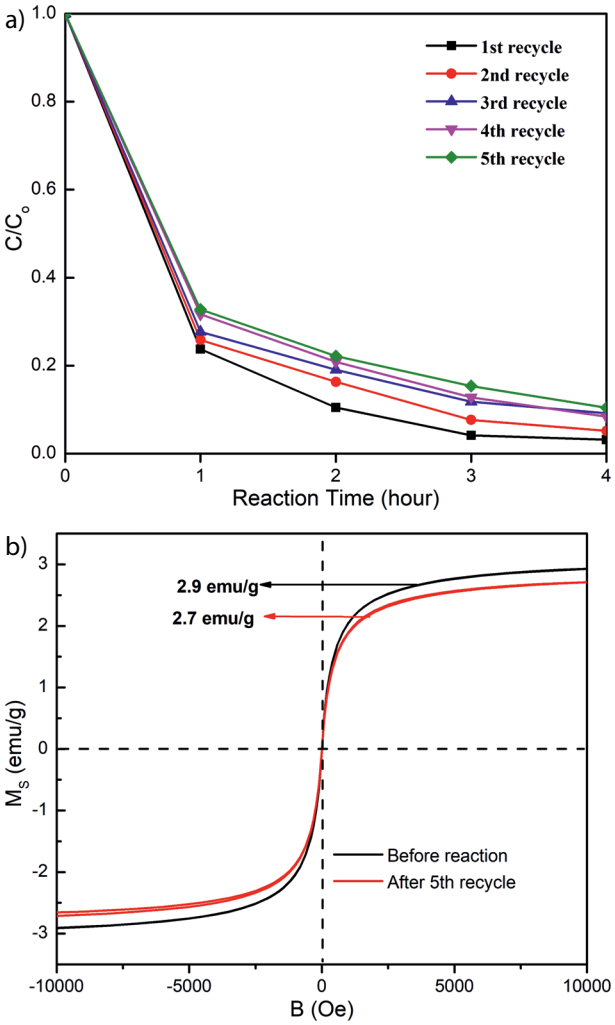

Figure 10. (a) Stability study on the photocatalytic degradation of a RR 195 solution over 40 % Ag_3PO_4/HAp@γ-Fe_2O_3 under simulated sunlight irradiation. (b) Magnetic hysteresis loops of 40 % Ag_3PO_4/HAp@γ-Fe_2O_3 before reaction and after five recycles. Reaction conditions: V_{sample} = 30 mL, $m_{photocatalyst}$ = 50 mg, 0.5 mL H_2O_2.

Based on the above discussion, the active species $^{\bullet}O_2^-$ and h^+ work together to degrade the MB and RR 195 dyes. The reactions are proposed as follows:

$$Ag_3PO_4/HAp@\gamma\text{-}Fe_2O_3 + \text{visible irradation} \rightarrow \bar{e}_{CB} + h^+_{VB} \quad (3)$$

$$\bar{e}_{CB} + O_2 \rightarrow {}^{\bullet}O_2 \quad (4)$$

$$^{\bullet}O_2^- + \text{dyes} \rightarrow \text{degradation products} \quad (5)$$

$$h^+ + \text{dyes} \rightarrow \text{degradation products} \quad (6)$$

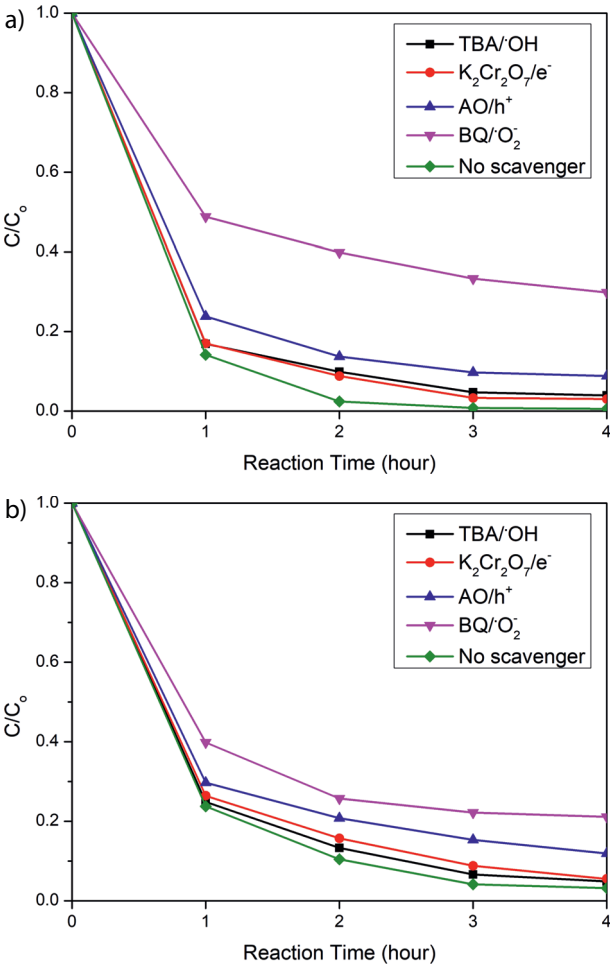

Figure 11. Trapping experiments of active species during the photocatalytic degradation of (a) MB and (b) RR 195 over the 40 % Ag_3PO_4/HAp@γ-Fe_2O_3 photocatalyst under visible light irradiation. Reaction conditions: V_{sample} = 30 mL, $m_{photocatalyst}$ = 50 mg, 0.5 mL H_2O_2.

4 Conclusions

As green photocatalyst, the Ag_3PO_4/HAp@γ-Fe_2O_3 composite with well-dispersed Ag_3PO_4 nanoparticles on magnetic HAp was successfully synthesized in aqueous solution via coprecipitation. Eggshells were used as the main source for the synthesis of HAp. The crystal structure, surface morphology, chemical state, optical properties, and recoverability by an external magnetic field were investigated by XRD, SEM, BET analysis, XPS, UV-vis DRS, and VSM. The Ag_3PO_4/HAp@γ-Fe_2O_3 samples exhibited high photocatalytic activity in degradation for both anionic and cationic dyes under visible light. The Ag_3PO_4/HAp@γ-Fe_2O_3 composite with its ease of fabrication, high photocatalytic activity, convenient recovery by magnet, and high reusability has potential as photocatalyst for practical applications in treating organic pollutants using direct solar energy.

Supporting Information

Supporting Information for this article can be found under DOI: https://doi.org/10.1002/ceat.202100261. This section includes additional references to primary literature relevant for this research [54–56].

The authors have declared no conflict of interest.

Abbreviations

AO	ammonium oxalate monohydrate
BET	Brunauer-Emmett-Teller
BJH	Barrett-Joyner-Halenda
BQ	1,4-benzoquinone
FT-IR	Fourier transform infrared
HAp	hydroxyapatite
MB	Methylene Blue
PL	photoluminance
PZC	point of zero charge
RR 195	Reactive Red 195
SEM	scanning electron microscopy
TBA	*tert*-butyl alcohol
TEM	transmission electron microscopy
UV-vis DRS	ultraviolet-visible light diffuse reflectance spectroscopy
VSM	vibrating sample magnetometry
XPS	X-ray photoelectron spectroscopy
XRD	X-ray diffraction

References

[1] I. Arslan, I. A. Balcioglu, Degradation of Remazol Black B dye and its simulated dyebath wastewater by advanced oxidation processes in heterogeneous and homogeneous media, *Color. Technol.* **2001**, *117 (1)*, 38–42. DOI: https://doi.org/10.1111/j.1478-4408.2001.tb00333.x

[2] M. Özacar, I. A. Şengil, Adsorption of reactive dyes on calcined alunite from aqueous solutions, *J. Hazard. Mater.* **2003**, *98 (1–3)*, 211–224. DOI: https://doi.org/10.1016/s0304-3894(02)00358-8

[3] G. Jayanthi Kalaivani, S. K. Suja, TiO_2 (rutile) embedded inulin – A versatile bio-nanocomposite for photocatalytic degradation of Methylene Blue, *Carbohydr. Polym.* **2016**, *143*, 51–60. DOI: https://doi.org/10.1016/j.carbpol.2016.01.054

[4] Z. Zhou, X. Peng, L. Zhong, L. Wu, X. Cao, R. C. Sun, Electrospun cellulose acetate supported Ag@AgCl composites with facet-dependent photocatalytic properties on degradation of organic dyes under visible-light irradiation, *Carbohydr. Polym.* **2016**, *136*, 322–328. DOI: https://doi.org/10.1016/j.carbpol.2015.09.009

[5] T. Yao, S. Guo, C. Zeng, C. Wang, L. Zhang, Investigation on efficient adsorption of cationic dyes on porous magnetic polyacrylamide microspheres, *J. Hazard. Mater.* **2015**, *292*, 90–97. DOI: https://doi.org/10.1016/j.jhazmat.2015.03.014

[6] S. D. Ashrafi, S. Rezaei, H. Forootanfar, A. H. Mahvi, M. A. Faramarzi, The enzymatic decolorization and detoxification of synthetic dyes by the laccase from a soil-isolated ascomycete, *Paraconiothyrium variabile, Int. Biodeterior. Biodegrad.* **2013**, *85*, 173–181. DOI: https://doi.org/10.1016/j.ibiod.2013.07.006

[7] A. Akhundi, A. Badiei, G. M. Ziarani, A. Habibi-Yangjeh, M. J. Muñoz-Batista, R. Luque, Graphitic carbon nitride-based photocatalysts: Toward efficient organic transformation for value-added chemicals production, *Mol. Catal.* **2020**, *488*, 110902. DOI: https://doi.org/10.1016/j.mcat.2020.110902

[8] T. G. Ambaye, K. Hagos, Photocatalytic and biological oxidation treatment of real textile wastewater, *Nanotechnol. Environ. Eng.* **2020**, *5*, 28. DOI: https://doi.org/10.1007/s41204-020-00094-w

[9] X. N. Pham, M. B. Nguyen, H. S. Ngo, H. V. Doan, Highly efficient photocatalytic oxidative desulfurization of dibenzothiophene with sunlight irradiation using green catalyst of Ag@AgBr/Al-SBA-15 derived from natural halloysite, *J. Ind. Eng. Chem.* **2020**, *90*, 358–370. DOI: https://doi.org/10.1016/j.jiec.2020.07.037

[10] X. N. Pham, H. T. Nguyen, T. N. Pham, T. T. B. Nguyen, B. M. Nguyen, V. T. T. Tran, H. V. Doan, Green synthesis of H-ZSM-5 zeolite-anchored O-doped g-C_3N_4 for photodegradation of Reactive Red 195 (RR 195) under solar light, *J. Taiwan Inst. Chem. Eng.* **2020**, *114*, 91–102. DOI: https://doi.org/10.1016/j.jtice.2020.09.018

[11] X. N. Pham, D. T. Pham, H. S. Ngo, M. B. Nguyen, H. V. Doan, Characterization and application of C-TiO_2 doped cellulose acetate nanocomposite film for removal of Reactive Red-195, *Chem. Eng. Commun.* **2020**, *208 (3)*, 304–317. DOI: https://doi.org/10.1080/00986445.2020.1712375

[12] Z. Yi, J. Ye, N. Kikugawa, T. Kako, S. Ouyang, H. S. Williams, H. Yang, J. Cao, W. Luo, Z. Li, Y. Liu, R. L. Withers, An orthophosphate semiconductor with photooxidation properties under visible-light irradiation, *Nat. Mater.* **2010**, *9 (7)*, 559–564. DOI: https://doi.org/10.1038/nmat2780

[13] A. Wu, C. Tian, W. Chang, Y. Hong, Q. Zhang, Y. Qu, H. Fu, Morphology-controlled synthesis of Ag_3PO_4 nano/microcrystals and their antibacterial properties, *Mater. Res. Bull.* **2013**, *48 (9)*, 3043–3048. DOI: https://doi.org/10.1016/j.materresbull.2013.04.054

[14] J. K. Liu, C. X. Luo, J. D. Wang, X. H. Yang, X. H. Zhong, Controlled synthesis of silver phosphate crystals with high photocatalytic activity and bacteriostatic activity, *CrystEngComm* **2012**, *14 (24)*, 8714–8721. DOI: https://doi.org/10.1039/C2CE25604E

[15] L. Xu, Q. Lang, Y. Zhao, W. Wang, H. Liu, R. Wang, Synthesis of Ag_3PO_4 nanospheres for significant photocatalytic activity under direct sunlight irradiation, *Ferroelectrics* **2017**, *515 (1)*, 127–133. DOI: https://doi.org/10.1080/00150193.2017.1367225

[16] X. Yang, H. Cui, Y. Li, J. Qin, R. Zhang, H. Tang, Fabrication of Ag_3PO_4-graphene composites with highly efficient and stable visible light photocatalytic performance, *ACS Catal.* **2013**, *3 (3)*, 363–369. DOI: https://doi.org/10.1021/cs3008126

[17] S. Bai, X. Shen, H. Lv, G. Zhu, C. Bao, Y. Shan, Assembly of Ag_3PO_4 nanocrystals on graphene-based nanosheets with enhanced photocatalytic performance, *J. Colloid Interface*

Sci. **2013**, *405*, 1–9. DOI: https://doi.org/10.1016/j.jcis.2013.05.023

[18] J. Ma, J. Zou, L. Li, C. Yao, T. Zhang, D. Li, Synthesis and characterization of Ag_3PO_4 immobilized in bentonite for the sunlight-driven degradation of Orange II, *Appl. Catal., B* **2013**, *134–135*, 1–6. DOI: https://doi.org/10.1016/j.apcatb.2012.12.032

[19] Q. Wu, P. Wang, F. Niu, C. Huang, Y. Li, W. Yao, A novel molecular sieve supporting material for enhancing activity and stability of Ag_3PO_4 photocatalyst, *Appl. Surf. Sci.* **2016**, *378*, 552–563. DOI: https://doi.org/10.1016/j.apsusc.2016.03.158

[20] Q. Wu, P. Wang, F. Niu, Y. Hong, M. Luo, W. Yao, Facile synthesis of $Ag_3PO_4/AlPO_{4\text{-}5}$ composite photocatalyst with enhanced visible-light-responded photocatalytic activities, *J. Taiwan Inst. Chem. Eng.* **2016**, *60*, 532–537. DOI: https://doi.org/10.1016/j.jtice.2015.09.018

[21] W. Zhai, G. Li, P. Yu, L. Yang, L. Mao, Silver phosphate/carbon nanotube-stabilized pickering emulsion for highly efficient photocatalysis, *J. Phys. Chem. C* **2013**, *117 (29)*, 15183–15191. DOI: https://doi.org/10.1021/jp404456a

[22] Q. Xiang, D. Lang, T. Shen, F. Liu, Graphene-modified nanosized Ag_3PO_4 photocatalysts for enhanced visible-light photocatalytic activity and stability, *Appl. Catal., B* **2015**, *162*, 196–203. DOI: https://doi.org/10.1016/j.apcatb.2014.06.051

[23] P. Chen, L. Zhang, Q. Wu, W. Yao, Novel synthesis of Ag_3PO_4/CNFs/silica-fiber hybrid composite as an efficient photocatalyst, *J. Taiwan Inst. Chem. Eng.* **2016**, *63*, 506–511. DOI: https://doi.org/10.1016/j.jtice.2016.03.029

[24] K. Elayaraja, P. Rajesh, M. I. A. Joshy, V. S. Chandra, R. V. Suganthi, J. Kennedy, P. K. Kulriya, I. Sulania, K. Asokan, D. Kanjilai, D. K. Avasthi, H. K. Varma, S. N. Kalkura, Enhancement of wettability and antibiotic loading/release of hydroxyapatite thin film modified by 100 MeV Ag^{7+} ion irradiation, *Mater. Chem. Phys.* **2012**, *134 (1)*, 464–477. DOI: https://doi.org/10.1016/j.matchemphys.2012.03.018

[25] D. Gopi, J. Indira, L. Kavitha, M. Sekar, U. K. Mudali, Synthesis of hydroxyapatite nanoparticles by a novel ultrasonic assisted with mixed hollow sphere template method, *Spectrochim. Acta, Part A* **2012**, *93*, 131–134. DOI: https://doi.org/10.1016/j.saa.2012.02.033

[26] M. Vila, T. Fernández-Lanas, B. González, M. Vallet-Regí, Macroporous sol-gel hydroxyapatite moulding via confinement into shaped acrylate-acrylamide copolymers, *J. Eur. Ceram. Soc.* **2012**, *32 (10)*, 2121–2127. DOI: https://doi.org/10.1016/j.jeurceramsoc.2012.01.034

[27] S. T. Ramesh, N. Rameshbabu, R. Gandhimathi, M. Srikanth Kumar, P. V. Nidheesh, Adsorptive removal of Pb(II) from aqueous solution using nano-sized hydroxyapatite, *Appl. Water Sci.* **2013**, *3 (1)*, 105–113. DOI: https://doi.org/10.1007/s13201-012-0064-z

[28] A. C. Dancu, R. Barabas, E. S. Bogya, Adsorption of nicotinic acid on the surface of nanosized hydroxyapatite and structurally modified hydroxyapatite, *Cent. Eur. J. Chem.* **2011**, *9 (4)*, 660–669. DOI: https://doi.org/10.2478/s11532-011-0057-z

[29] G. Li, L. Mao, Magnetically separable Fe_3O_4-Ag_3PO_4 submicrometre composite: Facile synthesis, high visible light-driven photocatalytic efficiency, and good recyclability, *RSC Adv.* **2012**, *2*, 5108–5111. DOI: https://doi.org/10.1039/C2RA20504A

[30] X. Guo, N. Chen, C. Feng, Y. Yang, B. Zhang, G. Wang, Z. Zhang, Performance of magnetically recoverable core-shell Fe_3O_4@ Ag_3PO_4/AgCl for photocatalytic removal of methylene blue under simulated solar light, *Catal. Commun.* **2013**, *38*, 26–30. DOI: https://doi.org/10.1016/j.catcom.2013.04.010

[31] J. G. Ibanez, M. Hernandez-Esparza, C. Doria-Serrano, A. Fregoso-Infante, M. M. Singh, The point of zero charge of oxides, in *Environmental Chemistry*, Springer, Berlin **2008**, 70–78. DOI: https://doi.org/10.1007/978-0-387-49493-7_5

[32] K. Huang, Y. Lv, W. Zhang, S. Sun, B. Yang, F. Chi, S. Ran, X. Liu, One-step synthesis of Ag_3PO_4/Ag photocatalyst with visible-light photocatalytic activity, *Mater. Res.* **2015**, *18 (5)*, 939–945. DOI: https://doi.org/10.1590/1516-1439.346614

[33] L. Gan, L. Xu, K. Qian, Preparation of core-shell structured $CoFe_2O_4$ incorporated Ag_3PO_4 nanocomposites for photocatalytic degradation of organic dyes, *Mater. Des.* **2016**, *109*, 354–360. DOI: https://doi.org/10.1016/j.matdes.2016.07.043

[34] M. Kwaśniak-Kominek, M. Manecki, J. Matusik, M. Lempart, Carbonate substitution in lead hydroxyapatite $Pb_5(PO_4)_3OH$, *J. Mol. Struct.* **2017**, *1147*, 594–602. DOI: https://doi.org/10.1016/j.molstruc.2017.06.111

[35] J. A. Ramos Guivar, E. A. Sanches, F. Bruns, E. Sadrollahi, M. A. Morales, E. O. López, F. J. Litterst, Vacancy ordered γ-Fe_2O_3 nanoparticles functionalized with nanohydroxyapatite: XRD, FTIR, TEM, XPS and Mössbauer studies, *Appl. Surf. Sci.* **2016**, *389*, 721–734. DOI: https://doi.org/10.1016/j.apsusc.2016.07.157

[36] L. An, X. Zhao, C. Xu, Z. Yan, Z. Yang, Z. Xu, Magnetically separable and recyclable γ-Fe_2O_3/HAp/Ag_3PO_4 composite microsheets: Fabrication, characterization, and photocatalytic performance, *Russ. J. Phys. Chem. A* **2019**, *93 (7)*, 1343–1348. DOI: https://doi.org/10.1134/S003602441907015X

[37] P. Dong, G. Hou, C. Liu, X. Zhang, H. Tian, F. Xu, X. Xi, R. Shao, Origin of activity and stability enhancement for Ag_3PO_4 photocatalyst after calcination, *Materials (Basel)* **2016**, *9 (12)*, 968–985. DOI: https://doi.org/10.3390/ma9120968

[38] B. Demri, D. Muster, XPS study of some calcium compounds, *J. Mater. Process. Technol.* **1995**, *55 (3–4)*, 311–314. DOI: https://doi.org/10.1016/0924-0136(95)02023-3

[39] E. O. López, A. Mello, H. Sendio, L. T. Costa, A. L. Rossi, R. O. Ospina, F. F. Borghi, J. G. S. Filho, A. M. Rossi, Growth of crystalline hydroxyapatite thin films at room temperature by tuning the energy of the RF-magnetron sputtering plasma, *ACS Appl. Mater. Interfaces* **2013**, *5 (19)*, 9435–9445. DOI: https://doi.org/10.1021/am4020007

[40] J. Blomquist, U. Helgeson, L. C. Moberg, B. Folkesson, R. Larsson, ESCA and Mössbauer spectra of some iron(III) betadiketonates and tetraphenylporphyrin iron(III) chloride, *Inorg. Chim. Acta* **1983**, *69*, 17–23. DOI: https://doi.org/10.1016/S0020-1693(00)83546-X

[41] Y. Li, H. Zhou, G. Shao, H. Pan, X. Xu, R. Tang, High efficient multifunctional Ag_3PO_4 loaded hydroxyapatite nanowires for water treatment, *J. Hazard. Mater.* **2015**, *299*, 379–387. DOI: https://doi.org/10.1016/j.jhazmat.2015.06.032

[42] P. Kubelka, F. Munk, Ein Beitrag zur Optik der Farbanstriche, *Z. Tech. Phys.* **1931**, *12*, 593–601.
[43] Y. Jiang, P. Liu, Y. Chen, Z. Zhou, H. Yang, Y. Hong, F. Li, L. Ni, Y. Yan, D. H. Gregroy, Construction of stable Ta_3N_5/*g*-C_3N_4 metal/non-metal nitride hybrids with enhanced visible-light photocatalysis, *Appl. Surf. Sci.* **2017**, *391*, 392–403. DOI: https://doi.org/10.1016/j.apsusc.2016.04.094
[44] S. Kour, R. K. Sharma, R. Jasrotia, V. P. Singh, A brief review on the synthesis of maghemite (γ-Fe_2O_3) for medical diagnostic and solar energy applications, *AIP Conf. Proc.* **2019**, *2142 (1)*, 090007. DOI: https://doi.org/10.1063/1.5122451
[45] J. Chen, X. Yang, C. Zhu, X. Xie, C. Lin, Y. Zhao, Q. Yan, A research on shape-controllable synthesis of Ag_3PO_4/AgBr and its degradation of ciprofloxacin, *Water Sci. Technol.* **2018**, *77 (5)*, 1230–1237. DOI: https://doi.org/10.2166/wst.2017.643
[46] X. Zhao, Y. Dong, B. Cheng, W. Kang, Removal of textile dyes from aqueous solution by heterogeneous photo-Fenton reaction using modified PAN nanofiber Fe complex as catalyst, *Int. J. Photoenergy* **2013**, *2013*, 820165. DOI: https://doi.org/10.1155/2013/820165
[47] M. P. Reddy, A. Venugopal, M. Subrahmanyam, Hydroxyapatite photocatalytic degradation of calmagite (an azo dye) in aqueous suspension, *Appl. Catal., B* **2007**, *69 (3–4)*, 164–170. DOI: https://doi.org/10.1016/j.apcatb.2006.07.003
[48] Z. Yang, X. Gong, C. Zhang, Recyclable Fe_3O_4/hydroxyapatite composite nanoparticles for photocatalytic applications, *Chem. Eng. J.* **2010**, *165 (1)*, 117–121. DOI: https://doi.org/10.1016/j.cej.2010.09.001
[49] S. Valizadeh, M. H. Rasoulifard, M. S. Seyed Dorraji, Modified Fe_3O_4-hydroxyapatite nanocomposites as heterogeneous catalysts in three UV, Vis and Fenton like degradation system, *Appl. Surf. Sci.* **2014**, *319*, 358–366. DOI: https://doi.org/10.1016/j.apsusc.2014.07.139
[50] B. Pare, S. B. Jonnalagadda, H. Tomar, P. Singh, V. W. Bhagwat, ZnO assisted photocatalytic degradation of Acridine Orange in aqueous solution using visible irradiation, *Desalination* **2008**, *232 (1–3)*, 80–90. DOI: https://doi.org/10.1016/j.desal.2008.01.007
[51] T. Chen, R. Doong, W. Lei, Photocatalytic degradation of parathion in aqueous TiO_2 dispersion: The effect of hydrogen peroxide and light intensity, *Water Sci. Technol.* **1998**, *37 (8)*, 187–194. DOI: https://doi.org/10.1016/s0273-1223(98)00249-2
[52] P. Zhu, Y. Chen, M. Duan, Z. Ren, M. Hu, Construction and mechanism of a highly efficient and stable *Z*-scheme Ag_3PO_4/reduced graphene oxide/Bi_2MoO_6 visible-light photocatalyst, *Catal. Sci. Technol.* **2018**, *8 (15)*, 3818–3832. DOI: https://doi.org/10.1039/c8cy01087k
[53] J. J. Buckley, A. F. Lee, L. Olivi, K. Wilson, Hydroxyapatite supported antibacterial Ag_3PO_4 nanoparticles, *J. Mater. Chem.* **2010**, *20 (37)*, 8056–8063. DOI: https://doi.org/10.1039/C0JM01500H
[54] M. Y. Rezk, M. Zeitoun, A. N. El-Shazly, M. M. Omar, N. K. Allam, Robust photoactive nanoadsorbents with antibacterial activity for the removal of dyes, *J. Hazard. Mater.* **2019**, *378 (15)*, 120679. DOI: https://doi.org/10.1016/j.jhazmat.2019.05.072
[55] D. Fu, G. Han, F. Liu, Y. Xiao, H. Wang, R. Liu, C. Liu, Visible-light enhancement of methylene blue photodegradation by graphitic carbon nitride-titania composites, *Mater. Sci. Semicond. Process.* **2014**, *27*, 966–974. DOI: https://doi.org/10.1016/j.mssp.2014.08.004
[56] O. Dyes, M. Blue, R. Bengal, U. Urea, D. N. Zno, N. Ahmad, Photocatalytic Degradation of the Light Sensitive, *Catalysts* **2020**, *10 (12)*, 1457–1473. DOI: https://doi.org/10.3390/catal10121457

